Research Square

Preprints are preliminary reports that have not undergone peer review.
They should not be considered conclusive, used to inform clinical practice,
or referenced by the media as validated information.

# Impact of grid resolution on turbulence representation in finite-volume simulations

**María Clara Cortizo Carbone**

claracortizo@fceia.unr.edu.ar

National University of Rosario

**Juan Cruz Catalano**

National University of Rosario

**César Martín Venier**

National University of Rosario

**Santiago Márquez Damián**

Centro de Investigación de Métodos Computacionales

**César Ignacio Pairetti**

National University of Rosario

**Research Article**

**Keywords:**

**Posted Date:** November 16th, 2026

**DOI:** https://doi.org/10.21203/rs.3.rs-11471619/v1

**License:** This work is licensed under a Creative Commons Attribution 4.0 International License.
Read Full License

**Additional Declarations:** No competing interests reported.

# Impact of grid resolution on turbulence representation in finite-volume simulations

**María Clara Cortizo Carbone · Juan Cruz Catalano · César M. Venier · Santiago Márquez Damián · César I. Pairetti**

**Abstract** Direct numerical simulation (DNS) aims to resolve all dynamically relevant turbulent scales without an explicit turbulence-closure model. In finite-volume methods (FVMs), representing the solution by cell averages introduces an effective spatial cutoff at the cell size. Here, a statistically stationary flow reproducing homogeneous isotropic turbulence (HIT) conditions is used to assess the effect of this cutoff. Fixed-grid calculations quantify the sensitivity of spectral and large-scale statistics to mesh resolution, while the analysis also considers kinetic energy, dissipation, thermodynamic equilibrium, and length-scale ratios. The results show that apparently adequate spectral resolution alone does not ensure statistically consistent turbulent dynamics. Adaptive mesh refinement (AMR) calculations use a local estimate of the Kolmogorov scale to examine information loss due to coarsening. For the present setup, particularly at low Reynolds number, only the conservative AMR threshold maintains maximum grid refinement throughout the simulation and therefore resolves the flow to the prescribed level. Less restrictive criteria cause temporal grid coarsening and reduce the accuracy of the turbulence statistics. These findings help characterize finite-volume grid requirements for DNS and the effects of spatial filtering on turbulent-flow simulations.

**Keywords** Direct numerical simulation · homogeneous isotropic turbulence · finite-volume method · grid resolution · adaptive mesh refinement

## 1 Introduction

Direct numerical simulation (DNS) denotes the numerical solution of the Navier–Stokes equations with sufficient spatial and temporal resolution to represent all dynamically relevant turbulent scales, without an explicit turbulence-closure model [11, 19, 23]. The absence of an explicit closure is therefore necessary but not sufficient: fidelity also depends on controlling discretization errors in space and time, as well as on the observables used to assess the computed flow [19, 33]. Every grid-based method implies a smallest represented length scale. In the context of a finite-volume method (FVM), the cell size $\Delta$ provides a natural measure of this cutoff because the numerical solution is represented by cell averages. Subcell fluctuations are not explicitly represented, and the discretization consequently acts as an implicit spatial filter [3, 29].

Unresolved turbulent scales influence the dynamics captured by the grid through interscale interactions, so their truncation can affect dissipation and resolved-flow statistics in ways that depend jointly on the mesh and numerical schemes, rather than on $\Delta$ alone [3, 19, 33]. In under-resolved DNS (UDNS) and large-eddy simulation (LES), the treatment of unresolved motions is therefore central to the fidelity of the resolved flow: wavelet-based adaptive implicit LES/UDNS exploits filtering-induced dissipation to represent their influence [5], while Taylor–Green vortex comparisons show that subgrid treatment modifies energy and enstrophy spectra [8]. Recent studies further address this coupling through characteristic length scales for anisotropic LES grids [31], small-scale velocity reconstruction [30], multiscale pseudo-DNS [9], and mixed subfilter-scale models [16]. Together, these studies highlight the importance of assessing how unresolved scales affect the represented dynamics, rather than judging resolution solely from the apparent spectral cutoff. This assessment is essential for high-fidelity

M. C. Cortizo Carbone, J. C. Catalano, C. M. Venier, and C. I. Pairetti
Universidad Nacional de Rosario, Facultad de Ciencias Exactas, Ingeniería y Agrimensura, Escuela de Ingeniería Mecánica, Rosario, Argentina
IFIR Instituto de Física de Rosario (UNR, CONICET), Rosario, Argentina
E-mail: claracortizo@fceia.unr.edu.ar

S. Márquez Damián
Centro de Investigación de Métodos Computacionales (UNL–CONICET), Colectora Ruta Nacional N° 168, km 0, Paraje El Pozo, Santa Fe, Argentina
Universidad Tecnológica Nacional, Facultad Regional Santa Fe, Santa Fe, Argentina

simulation (HFS) and adaptive mesh refinement (AMR), where spectral diagnostics must be complemented by checks of dissipation, forcing–dissipation balance, and large-scale statistics.

The present work complements these efforts by focusing on the resolved scales to characterize the impact of grid resolution on the implicit spatial filter. To this end, spectral analysis and integrated statistical diagnostics are used to study homogeneous isotropic turbulence (HIT). The scale distribution of this case is described using established quantities such as the energy spectrum, dissipation rate, Taylor-microscale Reynolds number, and integral length scales [12–14, 18, 28]. The Basilisk platform [24–26] provides a tree-based, second-order finite-volume implementation of a Navier–Stokes solver and is used here to compare small-scale resolution measures with global flow statistics.

The objective of this work is to quantify the impact that grid resolution has on flow-scale representation accuracy in Finite-Volume simulations, using a forced HIT case as benchmark. Section 2 describes the physical model, the case setup, and the numerical methods employed. Section 3 presents the complete description of the reference case, to verify the consistency with the reference results of [28]. Section 4 analyzes a more extensive range of flow regimes, grid resolutions, and adaptation strategies based on small-scale estimation, comparing the results for this diverse set of simulations in Section 5. The Conclusions of the aforementioned steps are presented in Section 6.

## 2 Physical Model and Numerical Method

### 2.1 Governing Equations

The flow dynamics is governed by the conservation equations of mass and linear momentum (Eqs. (1) and (2), respectively) for an incompressible Newtonian fluid of constant density:

$$\frac{\partial u_i}{\partial x_i} = 0 \tag{1}$$

$$\frac{\partial u_i}{\partial t} + u_j \frac{\partial u_i}{\partial x_j} = -\frac{1}{\rho}\frac{\partial p}{\partial x_i} + \frac{1}{\rho}\frac{\partial}{\partial x_j}(2\mu S_{ij}) + f_i \tag{2}$$

where $u_i$ are the velocity components, $p$ is the pressure, $S_{ij} = \frac{1}{2}\left(\frac{\partial u_i}{\partial x_j} + \frac{\partial u_j}{\partial x_i}\right)$ is the rate-of-strain tensor, and $f_i$ are the components of a body force. The fluid properties are the density $\rho$ and the dynamic viscosity $\mu$.

The nonlinear convective term $u_j \partial u_i/\partial x_j$ in Eq. (2) couples motions across a broad range of spatial and temporal scales and drives the turbulent energy cascade [7, 23]. Consequently, truncation at the grid scale can influence not only dissipative-range quantities but also global and large-scale statistics through nonlinear scale interactions.

### 2.2 Homogeneous Isotropic Turbulence Setup

A case of homogeneous isotropic turbulence in a cubic triply periodic domain of side length $L = 2\pi$ is analyzed. This benchmark allows the resolved spectra and statistics to be interpreted within the Kolmogorov framework as the grid resolution is varied. An "ABC"-type isotropic flow [22] is used as initial condition, with reference velocity $u_0 = 1$ m/s and characteristic wavenumber $k = 1$ m$^{-1}$.

In order to maintain turbulence in a statistically stationary state, a linear velocity-dependent forcing term is added [17], following the Basilisk tutorial configuration [1, 27, 28]. This mechanism is introduced directly into the governing equations as the body force components, denoted as $f_i$ in Eq. (2). Following the formulation in [27], this forcing term is written as:

$$f_i = A_0 \left(u_i - \langle u_i \rangle\right) \tag{3}$$

where $A_0$ is a parameter that controls the forcing intensity, set to $A_0 = 0.1$ for this study. The term within the parentheses represents the velocity fluctuation component, $u_i'$, defined as the difference between the local instantaneous cell velocity $u_i$ and the volume-averaged velocity over the entire domain $\langle u_i \rangle$.

The statistically stationary state of the forced HIT is characterized by several statistical metrics and turbulent scales. In the context of the present numerical simulations, the instantaneous volume-averaged turbulent kinetic energy, $\langle k \rangle(t)$, and viscous dissipation rate, $\langle \epsilon \rangle(t)$, are computed at every time step as:

$$\langle k \rangle(t) = \frac{1}{V}\int_V \frac{1}{2} u_i' u_i' \, dV \tag{4}$$

$$\langle \epsilon \rangle(t) = \frac{1}{V}\int_V \nu \left(\frac{\partial u_i}{\partial x_j}\frac{\partial u_i}{\partial x_j}\right) dV \tag{5}$$

where $V$ is the total volume of the cubic domain and $\nu$ is the kinematic viscosity. The intensity of these instantaneous velocity fluctuations is quantified by the root-mean-square velocity, defined as:

$$\langle u_{\mathrm{rms}} \rangle(t) = \sqrt{\frac{2}{3}\langle k \rangle} \tag{6}$$

Following the formulation in [28], a forcing-balance parameter, $A(t)$, can be evaluated dynamically to monitor the equilibrium between the injected energy by the linear forcing and the viscous dissipation:

$$A(t) = \frac{\langle \epsilon \rangle}{3\langle u_{\mathrm{rms}} \rangle^2} \tag{7}$$

In a statistically stationary state with balanced energy injection and dissipation, $A(t)$ is expected to fluctuate around the forcing coefficient $A_0 = 0.1$ imposed in Eq. (3). Once this regime is reached, an overline denotes a time average of the corresponding quantity. Under this framework, the characteristic integral length scale ($l$) and the turbulence eddy turnover time ($\tau$) are given by:

$$l = \frac{\langle u_{\mathrm{rms}} \rangle^3}{\langle \epsilon \rangle} \quad ; \quad \tau = \frac{\langle u_{\mathrm{rms}} \rangle^2}{\langle \epsilon \rangle} \tag{8}$$

Assuming that the normalized integral length scale converges asymptotically toward $l/L \approx 0.19$ for this specific linear forcing scheme, a relation for the forcing coefficient was established in [28], as written in Eq. (9).

$$A_0 = \frac{\overline{\langle \epsilon \rangle}^{1/3}}{0.99 L^{2/3}} \tag{9}$$

Here, this empirical relation is used before the simulations to derive predictive consistency targets. Given the prescribed forcing intensity $A_0$ and domain length $L$, the corresponding estimate of the statistically stationary dissipation rate is

$$\epsilon = (0.99 A_0)^3 L^2 \tag{10}$$

Combining this dissipation estimate with the definitions above gives consistency targets for the remaining statistical quantities as functions of $A_0$, $L$, and $\nu$. The root-mean-square velocity follows from Eqs. (7) and (9) as

$$u_{\mathrm{rms}} = \sqrt{\frac{(0.99 A_0)^3 L^2}{3 A_0}} \tag{11}$$

Substitution of Eqs. (10) and (11) into the Taylor-microscale definition yields

$$\lambda = \sqrt{15\frac{\nu}{\epsilon}}\, u_{\mathrm{rms}} = \sqrt{\frac{5\nu}{A_0}} \tag{12}$$

The corresponding Taylor-microscale Reynolds number is

$$Re_\lambda = \frac{u_{\mathrm{rms}}\, \lambda}{\nu} = \frac{1}{\nu}\sqrt{\frac{(0.99 A_0)^3 L^2}{3 A_0}\frac{5\nu}{A_0}} \tag{13}$$

The Kolmogorov length scale is estimated as

$$\eta = \left(\frac{\nu^3}{\epsilon}\right)^{1/4} \tag{14}$$

where $\nu$ is the kinematic viscosity and $\epsilon$ is the viscous dissipation rate.

This framework provides the predictive consistency targets summarized in Table 1 for the three kinematic viscosities considered. These estimates characterize the forcing configuration and are not a substitute for an independently converged DNS reference.

To systematically evaluate grid-resolution adequacy across these different turbulence intensities, a parametric study is conducted by varying the fluid kinematic viscosity ($\nu$) to achieve the three distinct target Reynolds numbers summarized above: $Re_\lambda = 25$, 80, and 145. For each physical configuration, the flow is subjected to different grid strategies, encompassing static uniform meshes and adaptive mesh refinement based on local Kolmogorov-scale resolution. Rather than performing a purely formal grid-convergence study, the present work examines which diagnostics remain reliable when the mesh is only partially adequate. This approach is intended to identify practical indicators of statistical fidelity for the present finite-volume solver.

Table 1: Predictive consistency targets for the main HIT quantities associated with the three viscosities considered, including $\epsilon$, $u_{\mathrm{rms}}$, $\lambda$, $Re_\lambda$, and $\eta$.

| $\nu$ | 0.01 | 0.001 | 0.0003 |
|---|---|---|---|
| $A$ | 0.1 | 0.1 | 0.1 |
| $L$ | $2\pi$ | $2\pi$ | $2\pi$ |
| $\epsilon$ | 0.03831 | 0.03831 | 0.03831 |
| $u_{\mathrm{rms}}$ | 0.3573 | 0.3573 | 0.3573 |
| $\lambda$ | 0.7071 | 0.2236 | 0.1225 |
| $Re_\lambda$ | 25 | 80 | 145 |
| $\eta$ | 0.07148 | 0.01271 | 0.00515 |

### 2.3 Solver algorithm and numerical schemes

The numerical simulations are performed with the open-source platform Basilisk [26], which solves multiphysics problems through the numerical integration of systems of partial differential equations. The incompressible Navier–Stokes equations are solved using a projection method [15, 24, 25]. This algorithm is based on the Finite Volume Method (FVM), where variables are defined at the cell centers. Space and time discretizations are both second-order accurate. The advective term is discretized with the Bell–Colella–Glaz advection scheme [2], while the viscous terms are treated with a fully implicit, second-order accurate diffusion scheme. The pressure-velocity coupling leads to a Poisson–Helmholtz equation, which is solved using a multigrid solver. The time step is dynamically adjusted to satisfy the CFL (Courant–Friedrichs–Lewy) condition [4], restricted to CFL = 0.8.

At the discrete level, the centered finite-volume projection method advances the flow variables by decoupling the velocity and pressure fields through a predictor-corrector sequence. First, an intermediate velocity field $\mathbf{U}^*$ is obtained by solving the momentum equation, neglecting the pressure gradient, where the advective and viscous terms are evaluated at the time level $n+\frac{1}{2}$:

$$\begin{aligned}\frac{\rho(\mathbf{U}^*-\mathbf{U}^n)}{\Delta t}+\nabla\cdot\left(\rho^{n+\frac{1}{2}}\,\mathbf{U}^{n+\frac{1}{2}}\mathbf{U}^{n+\frac{1}{2}}\right)\\ =\nabla\cdot[\mu^{n+\frac{1}{2}}(\mathbf{D}^n+\mathbf{D}^*)]+\mathbf{f}^{n+\frac{1}{2}},\end{aligned}\tag{15}$$

where $\mathbf{U}^n$ denotes the velocity at time $t_n$, $\rho$ is the density, $\mu$ is the dynamic viscosity, $\mathbf{D}$ is the strain-rate tensor, and $\mathbf{f}$ represents body forces. Since $\mathbf{U}^*$ does not generally satisfy the zero divergence, a pressure correction $p^{n+\frac{1}{2}}$ is computed by solving the following Poisson equation:

$$\nabla\cdot\left(\frac{\Delta t}{\rho^{n+\frac{1}{2}}}\nabla p^{n+\frac{1}{2}}\right)=\nabla\cdot\mathbf{U}^*\tag{16}$$

Finally, the divergence-free velocity field at the new time level $n+1$ is recovered via the projection step:

$$\mathbf{U}^{n+1}=\mathbf{U}^*-\frac{\Delta t}{\rho^{n+\frac{1}{2}}}\nabla p^{n+\frac{1}{2}}.\tag{17}$$

In the present single-phase incompressible setting, these expressions summarize the predictor, projection, and correction steps implemented in the solver. This procedure ensures mass conservation at every time step while maintaining second-order temporal and spatial accuracy.

### 2.4 Grid Strategies and Refinement Criteria

To evaluate the impact of spatial discretization on the resolving capability of the simulations, both fixed uniform grids and adaptive mesh refinement are considered. The tree-based grid hierarchy, fixed-grid layout, and AMR decision bounds are described in A.

In all cases, the local cell size $\Delta$ is dictated by the grid refinement level $\mathcal{L}$ through the relation $\Delta = L/2^{\mathcal{L}}$, where $L$ is the characteristic length of the computational domain. In the present study, maximum refinement levels of $\mathcal{L} = 7$, 8, and 9 are considered, which corresponds to equivalent uniform grid resolutions of $128^3$, $256^3$, and $512^3$ cells, respectively.

Fixed-grid simulations use a uniform mesh at constant refinement level $\mathcal{L}$. In the AMR simulations, the mesh is updated at every time step between $\mathcal{L}_{\min} = 3$ and $\mathcal{L}_{\max}$ according to the local Kolmogorov-scale criterion described below. The value of $\mathcal{L}_{\max}$ defines the finest available cell size and the corresponding uniform-grid resolution.

*Local Kolmogorov-scale refinement*

This physics-based criterion relates the cell size to the local Kolmogorov length scale $\eta_{\text{local}}$, following the definitions in A.2. The adaptive indicator is $\Delta_r = \Delta/\eta_{\text{local}}$. Its upper threshold, $\Delta_r^{\max}$, takes values of 1, 2, 4, and 8. The lower threshold is $\Delta_r^{\min} = \Delta_r^{\max}/c$, with $c = 4$ in all cases.

This criterion provides a resolution-based perspective complementary to wavelet-threshold approaches to adaptive turbulence simulation [5], by relating mesh adaptation directly to an estimate of the local dissipative scale.

### 2.5 Spectral Analysis and 3D FFT Diagnostics

In turbulent flows, the energy is transferred from the large injection scales down to the smallest dissipative scales through the energy cascade mechanism [12, 13, 23]. The three-dimensional energy spectrum, $E(\kappa)$, identifies the distribution of resolved energy across wavenumbers and provides a diagnostic of the inertial and dissipative ranges. The discrete Fourier transforms, velocity correlation tensor, and spherical integration procedure are described in B.

In this work, the energy spectrum is computed on the fly every 0.1 s of simulation time using an in-house parallel C implementation based on the FFTW library [6]. Since standard Fast Fourier Transform (FFT) algorithms strictly require a structured, uniformly spaced grid, a specialized data-sampling procedure is implemented depending on the underlying mesh strategy. For fixed uniform grids, the velocity components $u_i(\vec{x})$ are sampled directly at the cell centers of the mesh. Conversely, to overcome the spatial non-uniformity inherent to adaptive meshes (AMR), an auxiliary regular sampling grid is generated to match the uniform resolution corresponding to the maximum prescribed refinement level $\mathcal{L}_{max}$, using the same interpolation schemes employed to compute children cells in the AMR calculation; these uniform sampled points are the data employed for the 3D FFT.

## 3 Diagnostics, Statistical Metrics, and Fidelity Indicators

The spectral diagnostics introduced in Sec. 2.5 are combined with the global, integral, and small-scale quantities defined in Sec. 2.2 to assess consistency among the linear forcing, viscous dissipation, and large-scale dynamics of statistically stationary HIT.

The analysis is organized in three stages. First, a uniform-grid calculation at $\mathcal{L} = 7$ is compared with the published forced-HIT data to assess the internal consistency of the solver setup and post-processing diagnostics. Second, fixed-grid simulations are used to examine sensitivity to refinement level and Reynolds number. Finally, the best-resolved fixed-grid case at $Re_\lambda \approx 80$ is used as the internal numerical reference for the AMR fidelity and cost comparison.

### 3.1 Baseline case and internal consistency assessment

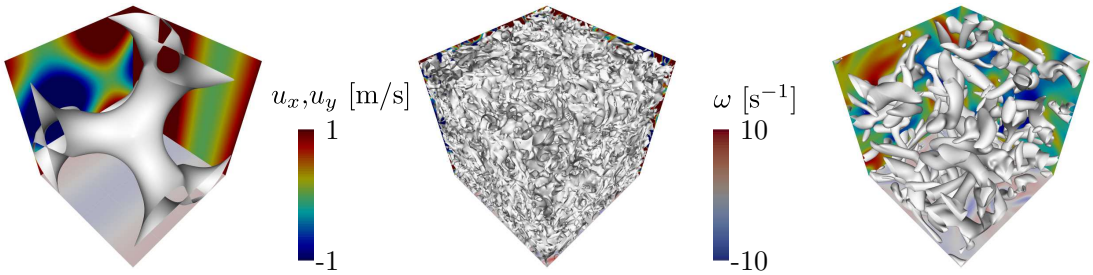
The baseline simulation uses a uniform $128^3$ grid, corresponding to $\mathcal{L} = 7$. Its parameters reproduce the statistically stationary HIT configuration reported in [28] and documented in the Basilisk example [1]. The kinematic viscosity is $\nu = 0.01\ \text{m}^2\,\text{s}^{-1}$ and the forcing coefficient is $A_0 = 0.1\ \text{s}^{-1}$. The resulting statistics are compared with the published data and with the predictive consistency targets in Table 1. This comparison is an internal assessment of the present setup and diagnostics, not an independent DNS validation.

The dynamic transition of the flow from the initial conditions to the fully developed turbulent statistically stationary regime can be interpreted by analyzing both the spatial morphology of the vortical structures, visualized using the $\lambda_2$-criterion [10] with $\lambda_2 = -1$ (Fig. 1), and the time histories of the global flow statistics (Fig. 2), namely the mean turbulent kinetic energy $\langle k \rangle$ and the mean viscous dissipation rate $\langle \epsilon \rangle$ defined in Eqs. (4) and (5), respectively.

Starting from the initial smooth velocity field at $t = 0$ s, the linear forcing continuously injects kinetic energy into the domain. The initial increase in kinetic energy is followed by a peak in viscous dissipation at $t \approx 20$ s in Fig. 2. This transient is associated with the stretching and breakdown of the initial large-scale structures into smaller vortices, as illustrated in Fig. 1(b).

Following this transient, the injected and dissipated energy approach a statistical balance. The late-time field in Fig. 1(c) illustrates the spatially homogeneous turbulent state at $t = 75$ s.

The late-time signals in Fig. 2 fluctuate around approximately constant means, consistently with the published pseudo-spectral data [1]. A 60 s moving-average window is used to expose these trends, as described in C. Table 2 reports averages over $t \geq 70$ s and compares them with the predictive consistency targets for $\nu = 0.01\ \text{m}^2\,\text{s}^{-1}$.




(a) t = 0 s (b) t = 20 s (c) t = 75 s

Fig. 1 Snapshots of the reference HIT simulation at successive times, showing the progressive distortion, stretching and breakdown of vortical structures as the flow reaches a statistically stationary state.

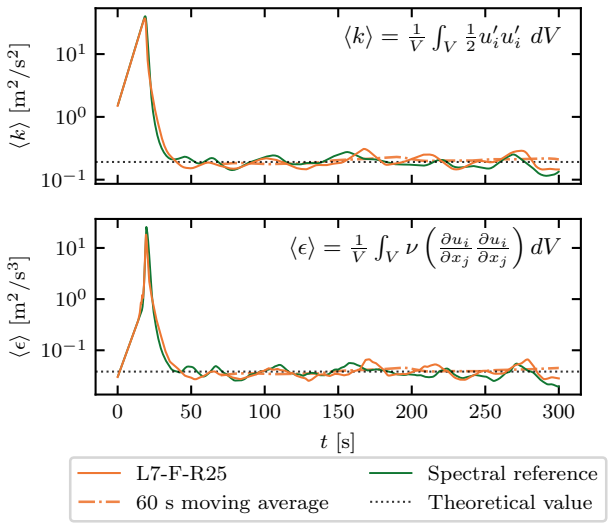



Fig. 2 Temporal evolution of volume-averaged kinetic energy $\langle k \rangle$ (top) and dissipation rate $\langle \epsilon \rangle$ (bottom) for L7-F-R25. The 60 s moving average characterizes the statistically stationary regime ($t \geq 70$ s). Results are compared with published pseudo-spectral data and predictive consistency targets.

Table 2: Time-averaged statistics of $\langle k \rangle$, $\langle \epsilon \rangle$, $A$, $l/L$, and $Re_\lambda$ for the baseline internal-consistency case over $t \geq 70$ s. Targets are the predictive estimates in Table 1 for $\nu = 0.01$ m$^2$ s$^{-1}$.

| Parameter | L7-F-R25 | Target (Table 1) | Error % |
|---|---|---|---|
| $\langle k \rangle$ | 0.20011 | 0.19153 | 4.48 % |
| $\langle \epsilon \rangle$ | 0.03891 | 0.03831 | 1.57 % |
| $A$ | 0.097 | 0.100 | 3.00 % |
| $l/L$ | 0.201 | 0.190 | 5.79 % |
| $Re_\lambda$ | 26.21 | 25.00 | 4.84 % |
| $\int E(\kappa)\, d\kappa$ | 0.19656 | 0.19153 | 2.63 % |
| $\int 2\nu\kappa^2 E(\kappa)\, d\kappa$ | 0.03711 | 0.03831 | 3.13 % |

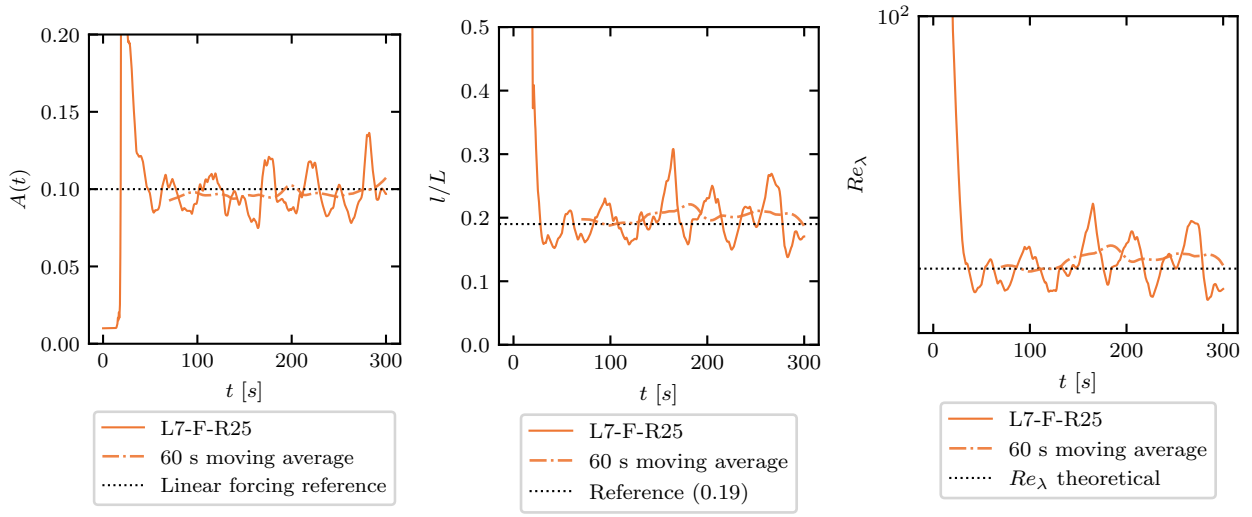
The time-averaged quantities in Table 2 differ from their predictive targets by less than 6%. Together with the agreement of the time histories in Fig. 2, this result supports the use of L7-F-R25 as an internal consistency check for the setup and post-processing procedure.

In addition to the energy and dissipation histories, three complementary indicators characterize the approach to a statistically stationary state: the forcing-balance parameter $A(t)$, the normalized balance-based length scale $l(t)/L$, and the Taylor-microscale Reynolds number $Re_\lambda(t)$.

Figure 3a shows $A(t)$, computed from the domain-averaged dissipation and root-mean-square velocity using Eq. (7). After the initial transient, $A(t)$ fluctuates around the forcing target, indicating statistical consistency between energy injection and viscous dissipation.

The balance-based length scale $l$ from Eq. (8) provides a complementary large-scale measure. In Fig. 3b, $l/L$ fluctuates around the value 0.19 reported for this forcing configuration in [28].

The Taylor-microscale Reynolds number in Fig. 3c shows the same transition toward a stationary range. Collectively, these indicators support the use of the baseline simulation as an internal consistency case, while the better-resolved L9-F-R80 simulation is retained as the numerical reference for the AMR comparisons.




(a) Forcing-balance parameter $A(t)$

(b) Normalized length scale $l/L$

(c) Taylor-microscale Reynolds number $Re_\lambda$

Fig. 3 Temporal evolution of complementary turbulent indicators for the baseline uniform simulation. The late-time behavior of the three metrics is consistent with the target statistically stationary state.

The spectral post-processing is assessed using the non-dimensional energy spectrum of L7-F-R25 in Fig. 4. The normalization uses the predictive dissipation estimate from Eq. (10), yielding $\kappa\eta$ and $E(\kappa)/(\epsilon\nu^5)^{1/4}$. The result is compared with the numerical data in [28] at a similar $Re_\lambda$. The Kolmogorov $-5/3$ law is included only as a qualitative reference because the moderate Reynolds number limits the extent of the inertial range.

The spectrum follows the published data over the resolved wavenumber range. It represents the energy-containing scales at low $\kappa\eta$, follows the available inertial-range trend, and exhibits the expected dissipative drop-off as $\kappa\eta$ approaches unity. This comparison supports use of the spectral pipeline as a comparative diagnostic, subject to the additional interpolation required for AMR fields.

The consistency between physical-space and spectral quantities is quantified through the energy and dissipation integrals. For statistically stationary HIT, the three-dimensional energy spectrum satisfies

$$\int_0^{\kappa_{\max}} E(\kappa)\, d\kappa = \overline{\langle k \rangle} \tag{18}$$

$$\int_0^{\kappa_{\max}} 2\nu\kappa^2 E(\kappa)\, d\kappa = \overline{\langle \epsilon \rangle} \tag{19}$$

where $\overline{\langle k \rangle}$ and $\overline{\langle \epsilon \rangle}$ denote the double time-space averages of turbulent kinetic energy and dissipation rate computed over the statistically stationary regime ($t \geq 70$ s), respectively.

For L7-F-R25, the integrated spectrum recovers more than 97% of the physical-space energy and approximately 97% of the physical-space dissipation. The corresponding differences relative to the predictive targets are reported in Table 2.

## 4 Results

Fixed-grid results are examined first for refinement levels $\mathcal{L} = 7, 8, 9$ and target Reynolds numbers $Re_\lambda \approx 25, 80, 145$. The AMR analysis then compares four thresholds of the local Kolmogorov-scale criterion against the best-resolved fixed-grid case available at $Re_\lambda \approx 80$.

All simulated cases considered in this manuscript are summarized in Table 3. Throughout the subsequent discussion, the predictive consistency targets serve as baselines, while the highest-resolution fixed-grid case ($\mathrm{L9-F-R80}$) provides the internal numerical benchmark for evaluating the convergence under adaptive mesh refinement.

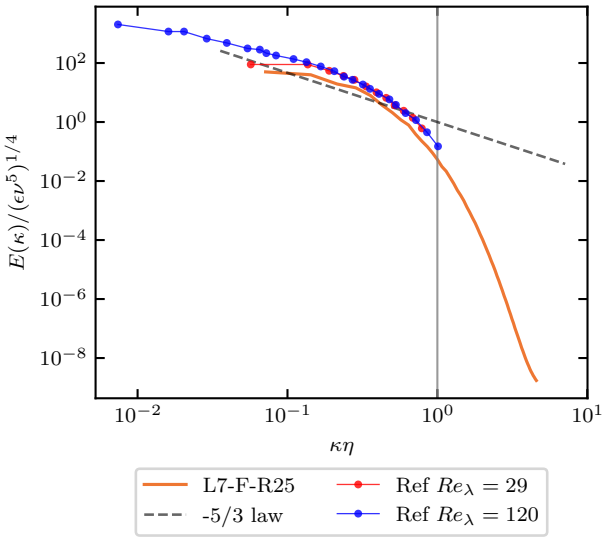



Fig. 4 Energy spectrum for the baseline case, illustrating the FFT-based post-processing procedure and comparison with published reference data.

Table 3: Summary of the numerical simulations executed in this work, including fixed-grid and adaptive mesh refinement configurations. The parameter $\Delta_r^{\max}$ denotes the AMR refinement threshold.

| Code[a] | $\mathcal{L}_{\max}$ | Viscosity $\nu$ | Mesh Type | Threshold ($\Delta_r^{\max}$) | $Re_\lambda$ |
|---|---|---|---|---|---|
| *Fixed-grid simulations* | | | | | |
| L7-F-R25 | 7 | 0.01 | Fixed | — | 25 |
| L7-F-R80 | 7 | 0.001 | Fixed | — | 80 |
| L8-F-R80 | 8 | 0.001 | Fixed | — | 80 |
| L9-F-R25 | 9 | 0.01 | Fixed | — | 25 |
| L9-F-R80[b] | 9 | 0.001 | Fixed | — | 80 |
| L9-F-R145 | 9 | 0.0003 | Fixed | — | 145 |
| *Adaptive Mesh Refinement (AMR) simulations* | | | | | |
| L9-AV1-R80 | 9 | 0.001 | AMR | 1 | 80 |
| L9-AV2-R80 | 9 | 0.001 | AMR | 2 | 80 |
| L9-AV4-R80 | 9 | 0.001 | AMR | 4 | 80 |
| L9-AV8-R80 | 9 | 0.001 | AMR | 8 | 80 |

[a] Code convention: L[$\mathcal{L}_{\max}$]-[mesh type/criterion]-R[$Re_\lambda$ target]. F: fixed grid; AV: AMR based on the local Kolmogorov scale.
[b] L9-F-R80 closes the grid-refinement study, provides the Reynolds-number baseline, and is the fixed-grid reference for the AMR comparison.

## 4.1 Results in fixed-grid simulations

The first part of the analysis evaluates the performance of uniform fixed grids. As summarized in the upper block of Table 3, these simulations encompass three maximum refinement levels ($\mathcal{L}_{\max} = 7, 8, 9$) and three viscosity values ($\nu = 0.01, 0.001, 0.0003$ m$^2$s$^{-1}$), corresponding to target Taylor-scale Reynolds numbers $Re_\lambda \approx 25, 80$, and 145.

To establish a quantitative baseline for subsequent AMR evaluations, Table 4 summarizes the computational performance and execution costs of all fixed-grid configurations. Across all cases, parallel performance remains consistent, with solver speeds hovering around $(6.7\text{–}8.6) \times 10^6$ pts/s/core and spectral transform overhead (FFT) accounting for less than 3.5% of the total clock time. These uniform-grid metrics define the benchmark computational effort required across the varying spatial resolutions and Reynolds numbers.

### *4.1.1 Influence of refinement in fixed-grid simulations*

Table 5 compares the predictive consistency targets and simulation-averaged values of $Re_\lambda$, $l/L$, and $\Delta/\eta$ for a viscosity $\nu = 0.001$ m$^2$s$^{-1}$ across grid levels 7, 8, and 9. The relative percentage error is calculated with respect to the target value. Similarly, Figure 5a displays the energy spectrum for the same viscosity and mesh levels. According to Pope's guideline for DNS [23], a resolution of $\Delta/\eta \approx 2.1$ is commonly associated with adequate representation of the dissipative scales. This rule corresponds approximately to the spectral resolution condition

Table 4: Summary of computational performance and cost metrics for fixed-grid simulations running on 64 MPI processes up to $t = 300.0$. Mean active cells are given in $10^6$. Speed values are given in $\frac{\text{pts}}{\text{s·core}}$.

| Code | Cells | Steps | Time (h) | FFT (h) | % FFT | Speed |
|---|---|---|---|---|---|---|
| *Fixed-grid simulations* | | | | | | |
| L7-F-R25 | 2.1 | 15324 | 1.30 | 0.05 | 3.35% | 6.73e6 |
| L7-F-R80 | 2.1 | 16810 | 1.50 | 0.04 | 2.65% | 6.78e6 |
| L8-F-R80 | 16.8 | 35093 | 19.90 | 0.34 | 1.70% | 8.28e6 |
| L9-F-R25 | 134.2 | 53774 | 245.40 | 2.80 | 1.14% | 8.41e6 |
| L9-F-R80 | 134.2 | 68752 | 318.30 | 2.88 | 0.90% | 8.61e6 |
| L9-F-R145 | 134.2 | 76496 | 345.50 | 2.86 | 0.83% | 8.48e6 |

$k_{\max}\eta \geq 1.5$ in wavenumber space, which is intended to avoid artificial truncation of the smallest dynamically relevant scales.

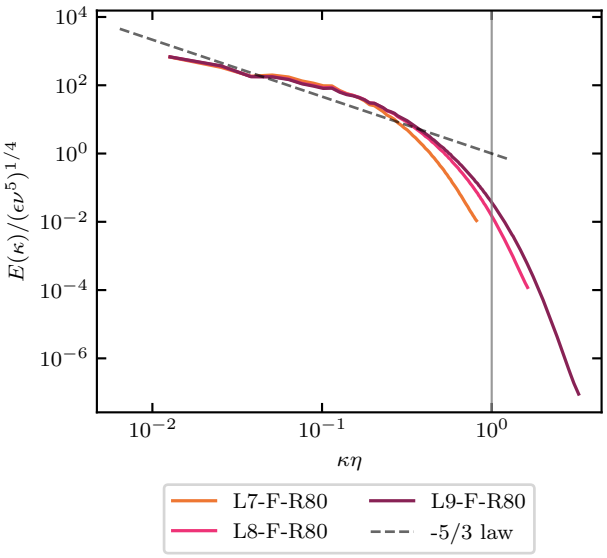
A joint analysis of both the table and the spectrum indicates that, in geometric terms, the level-8 mesh (L8-F-R80) reaches this conventional threshold, with resolved wavenumbers extending to $k\eta \geq 10^0$. The integrated spectral energy $\int E(\kappa)d\kappa$ also agrees closely with the physical-space kinetic-energy average, yielding relative differences below 0.25% for all grid levels. This reflects the fact that turbulent kinetic energy is primarily contained in large, low-wavenumber motions; it does not, by itself, certify convergence of the full turbulent dynamics.

Table 5: Comparison between predictive consistency targets, simulation-averaged turbulence parameters, and integrated spectral observables for $t \geq 70$ s and $\nu = 0.001$ m$^2$s$^{-1}$ across the three grid refinement levels ($\mathcal{L} = 7, 8, 9$).

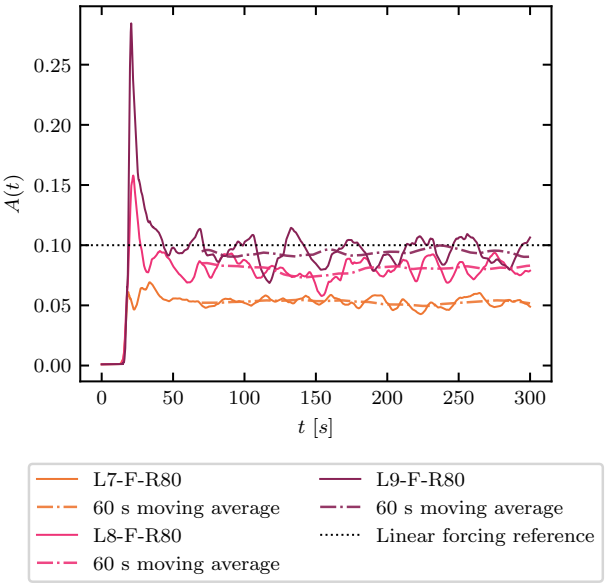
| Parameter | | $\mathcal{L}7$ | $\mathcal{L}8$ | $\mathcal{L}9$ |
|---|---|---|---|---|
| $\langle k \rangle$ | Theo. | 0.19153 | 0.19153 | 0.19153 |
| | Num. | 0.19342 | 0.19716 | 0.19439 |
| | Error % | 0.99 | 2.94 | 1.49 |
| $\langle \epsilon \rangle$ | Theo. | 0.03831 | 0.03831 | 0.03831 |
| | Num. | 0.02023 | 0.03129 | 0.03661 |
| | Error % | 47.18 | 18.32 | 4.43 |
| $A$ | Theo. | 0.100 | 0.100 | 0.100 |
| | Num. | 0.053 | 0.080 | 0.094 |
| | Error % | 47.00 | 20.00 | 6.00 |
| $l/L$ | Theo. | 0.190 | 0.190 | 0.190 |
| | Num. | 0.364 | 0.242 | 0.206 |
| | Error % | 91.58 | 27.37 | 8.42 |
| $Re_\lambda$ | Theo. | 79.9 | 79.9 | 79.9 |
| | Num. | 110.7 | 90.5 | 83.5 |
| | Error % | 38.61 | 13.30 | 4.45 |
| $\Delta/\eta$ | Theo. | 3.862 | 1.931 | 0.965 |
| | Num. | 3.292 | 1.836 | 0.954 |
| | Error % | 14.75 | 4.93 | 1.16 |
| $\int E(\kappa)\, d\kappa$ | Theo. | 0.19153 | 0.19153 | 0.19153 |
| | Num. | 0.19121 | 0.19198 | 0.19172 |
| | Error % | 0.17 | 0.24 | 0.10 |
| $\int 2\nu\kappa^2 E(\kappa)\, d\kappa$ | Theo. | 0.03831 | 0.03831 | 0.03831 |
| | Num. | 0.02346 | 0.03293 | 0.03690 |
| | Error % | 38.76 | 14.05 | 3.67 |

Figure 5b shows the temporal evolution of the parameter $A(t)$ relative to the forcing value $A_0$. The simulation-averaged values increase from 0.053 at level 7 to 0.080 at level 8 and 0.094 at level 9, compared with $A_0 = 0.100$ s$^{-1}$ (Table 5). Thus, the improvement in the level-8 spectrum is accompanied by a remaining 20% discrepancy in the forcing-balance parameter, reduced to 6% at level 9.

This resolution sensitivity is quantitatively confirmed by the simulation-averaged turbulence parameters presented in Table 5. When examining the time-averaged integral scales and Reynolds numbers for $t \geq 70$ s, the lower-resolution grids (levels 7 and 8) do not stabilize as close to the predictive consistency targets as level 9. Even though refining the mesh from level 7 to level 8 significantly improves the description of the dissipative range, bringing the error in $\Delta/\eta$ below 5%, the large-scale indicators remain biased. Both under-resolved grids exhibit substantial discrepancies in their integral parameters, with relative errors for $Re_\lambda$ and $l/L$ remaining large.




(a) The comparison of the energy spectra shows how refinement modifies the dissipative cutoff and the representation of the resolved turbulent cascade.




(b) Temporal evolution of the forcing-balance parameter $A(t)$ for the three fixed-grid resolutions.

Fig. 5 Comparison of a) the energy spectra and b) temporal evolution of $A(t)$, using three fixed-grid resolutions at levels 7, 8, and 9 for the intermediate-Reynolds-number case with $\nu = 0.001$ m$^2$s$^{-1}$.

The comparison between physical-space and spectral estimates of dissipation also illustrates the sensitivity of dissipation diagnostics to grid resolution. As shown at the bottom of Table 5, the spectral estimate $\int 2\nu\kappa^2 E(\kappa)\, d\kappa$ displays smaller discrepancies than the gradient-based estimate $\langle\epsilon\rangle$ on the coarser grids. This should not be interpreted as making the spectral estimate a more exact reference; rather, it shows that different dissipation diagnostics respond differently to under-resolution.

At level 9, the relative errors for $Re_\lambda$ and the balance-based length-scale ratio $l/L$ decrease to 4.45% and 8.42%, respectively. The error in the spatial resolution ratio $\Delta/\eta$ is 1.16%, showing that the residual discrepancies differ across these observables.

### *4.1.2 Changing Re at fixed mesh resolution*

The level-9 fixed grid is used to analyze three different physical cases obtained by varying the viscosity $\nu$, and therefore the characteristic Taylor-microscale Reynolds number $Re_\lambda$. Reducing the viscosity increases the separation between energy-containing and dissipative scales, making the level-9 grid progressively less adequate. Table 6 compares the predictive consistency targets for $Re_\lambda$, $l/L$, and $\Delta/\eta$ with their numerical counterparts, computed by averaging the simulation data over the statistically stationary regime ($t \geq 70$ s).

For the two higher-viscosity cases, corresponding to nominal Reynolds numbers of $Re_\lambda = 25$ (case L9-F-R25) and $Re_\lambda = 80$ (case L9-F-R80), the numerical results show close agreement with the predictive targets. Across all three parameters, the relative percentage errors remain below 5% for the lowest Reynolds number and within acceptable bounds for the intermediate case, where the largest deviation is 8.42% in the macroscale ratio $l/L$. This indicates that, for the present diagnostics and averaging window, the level-9 mesh provides adequate resolution for these two regimes.

Conversely, a marked degradation in accuracy is observed for the lowest-viscosity case (L9-F-R145). In this regime, the simulation overpredicts both $Re_\lambda$ and the length-scale ratio $l/L$, resulting in relative errors of 27.52% and 53.16%, respectively. This increase indicates that the fixed level-9 grid is no longer sufficient for this Reynolds-number range. Notably, the relatively small error in the estimated $\Delta/\eta$ value (5.97%) does not guarantee convergence of the remaining statistical parameters. The absolute resolution level, $\Delta/\eta \approx 2.24$, must therefore be interpreted together with the global balance and large-scale indicators.

This resolution limitation and its impact on the macro-statistics are reflected in the energy spectra presented in Figure 6a. As $Re_\lambda$ increases, the spectrum shifts toward lower non-dimensional wavenumbers, reflecting the broadening of the dynamically active scales and the expansion of the inertial range. For the L9-F-R25 and L9-F-R80 cases, the spectra show good agreement in the dissipative range ($\kappa\eta \approx 1$), consistent with the lower errors documented in Table 6. In contrast, the spectrum for the L9-F-R145 case departs from the lower-Reynolds-number curves as it approaches the dissipative zone. Although the simulation reaches the early dissipation range ($\kappa\eta \approx 1$), this coverage is insufficient to recover the global statistics of the flow with comparable accuracy.

Table 6: Comparison between predictive consistency targets, simulation-averaged turbulence parameters, and integrated spectral observables for $t \geq 70$ s using the level-9 fixed grid across three different viscosities of $\nu = 0.01,\ 0.001,\ 0.0003\ \mathrm{m^2 s^{-1}}$.

| Parameter | | 0.01 | 0.001 | 0.0003 |
|---|---|---|---|---|
| $\langle k \rangle$ | Theo. | 0.19153 | 0.19153 | 0.19153 |
| | Num. | 0.17829 | 0.19439 | 0.21569 |
| | Error % | 6.91 | 1.49 | 12.61 |
| $\langle \epsilon \rangle$ | Theo. | 0.03831 | 0.03831 | 0.03831 |
| | Num. | 0.03566 | 0.03661 | 0.02985 |
| | Error % | 6.92 | 4.43 | 22.09 |
| $A$ | Theo. | 0.100 | 0.100 | 0.100 |
| | Num. | 0.099 | 0.094 | 0.069 |
| | Error % | 1.00 | 6.00 | 31.00 |
| $l/L$ | Theo. | 0.190 | 0.190 | 0.190 |
| | Num. | 0.185 | 0.206 | 0.291 |
| | Error % | 2.63 | 8.42 | 53.16 |
| $Re_\lambda$ | Theo. | 25.00 | 80.00 | 146.00 |
| | Num. | 24.40 | 83.46 | 186.03 |
| | Error % | 3.43 | 4.45 | 27.52 |
| $\Delta/\eta$ | Theo. | 0.17168 | 0.96544 | 2.38169 |
| | Num. | 0.16864 | 0.95426 | 2.23939 |
| | Error % | 1.77 | 1.16 | 5.97 |
| $\int E(\kappa)\, d\kappa$ | Theo. | 0.19153 | 0.19153 | 0.19153 |
| | Num. | 0.17521 | 0.19172 | 0.21490 |
| | Error % | 8.52 | 0.10 | 12.20 |
| $\int 2\nu\kappa^2 E(\kappa)\, d\kappa$ | Theo. | 0.03831 | 0.03831 | 0.03831 |
| | Num. | 0.03347 | 0.03690 | 0.03269 |
| | Error % | 12.63 | 3.67 | 14.65 |

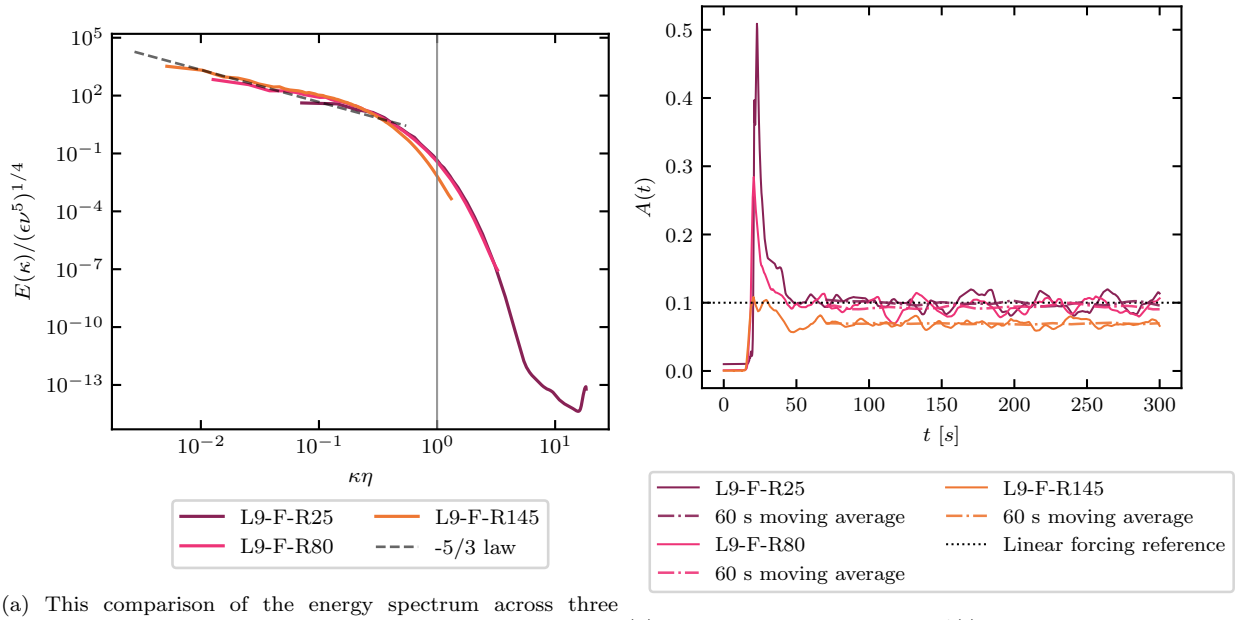
This loss of small-scale accuracy has direct consequences for the global energy balance of the system, as evidenced by the temporal evolution of the parameter $A(t)$ in Figure 6b. For the better-resolved cases (L9-F-R25 and L9-F-R80), once the initial transient phase passes ($t \geq 70$ s), $A(t)$ successfully converge and fluctuate close to the forcing target ($A_0 = 0.1$). This indicates that the grid is fine enough, for these cases, to establish a statistical equilibrium between the energy injected by the forcing mechanism and the energy dissipated at the small scales. Conversely, for the L9-F-R145 case, $A(t)$ stabilizes at a lower plateau, failing to achieve the expected balance. This offset is consistent with the resolution limitations previously observed in both the table and the energy spectra.

## 4.2 On the impact of local grid resolution

The adaptive mesh refinement (AMR) cases are compared against the best-resolved fixed-grid case available in this dataset (L9-F-R80) at the same target Reynolds number ($Re_\lambda \approx 80$), corresponding to the lower block of cases in Table 3. The comparison quantifies how the adaptation threshold changes the resolved statistics and computational cost.

The objective is to isolate the effect of relaxing the local resolution threshold within a single physics-based refinement strategy. Because statistically stationary HIT is globally homogeneous, AMR is not inherently expected to yield the large speedups typical of strongly localized, intermittent, or multiphase flows. Consequently, dynamic cell counts are reported to quantify the spatial adaptation fidelity, rather than as universal indicators of computational speedup.

To provide a quantitative baseline, Table 7 details the computational performance and execution costs of the AMR configurations in direct comparison to the fixed-grid reference (L9-F-R80). The metrics reflect the trade-off inherent to dynamic adaptation in homogeneous turbulence: conservative thresholds ($\Delta_r^{\max} = 1, 2$) retain nearly the full active cell count (134.2–$126.9 \times 10^6$ cells) while incurring tree-management overheads that increase total time up to 592.4 h. Conversely, relaxing the threshold ($\Delta_r^{\max} = 4, 8$) enforces aggressive spatial compression, reducing mean active cells down to 28.5% and 10.1% of the full grid, respectively, and lowering the time down to 46.9 h. However, as analyzed below, this reduction in computational effort comes at the expense of local resolution and directly impacts the accuracy of turbulent statistics. Across all configurations, FFT-based post-processing remains a minor contribution ($< 3\%$ of execution time).




(a) This comparison of the energy spectrum across three Reynolds-number regimes shows how higher $Re_\lambda$ broadens the active range of turbulent scales.

(b) The temporal evolution of $A(t)$ shows that increasing the Reynolds number makes the convergence of global statistics more demanding even when the spectrum appears resolved.

Fig. 6 Comparison of a) the energy spectra and b) temporal evolution of $A(t)$, for the level-9 fixed grid with viscosities $\nu = 0.01$ m$^2$s$^{-1}$, 0.001 m$^2$s$^{-1}$, and 0.0003 m$^2$s$^{-1}$.

Table 7: Summary of computational performance and cost metrics for fixed-grid and AMR simulations running on 64 MPI processes up to $t = 300$ s. Mean active cells are given in $10^6$. Speeds are given in $\frac{\text{pts}}{\text{s·core}}$.

| Code | Cells | Steps | Time (h) | FFT (h) | % FFT | Speed |
|---|---|---|---|---|---|---|
| *Fixed-grid simulation* | | | | | | |
| L9-F-R80 | 134.2 | 68752 | 318.32 | 2.88 | 0.90% | 8.61e6 |
| *Adaptive Mesh Refinement (AMR) simulations* | | | | | | |
| L9-AV1-R80 | 134.2 | 70064 | 402.8 | 3.0 | 0.75% | 6.95e6 |
| L9-AV2-R80 | 126.9 | 72060 | 592.4 | 2.8 | 0.48% | 5.25e6 |
| L9-AV4-R80 | 38.2 | 52833 | 175.6 | 1.7 | 0.97% | 3.68e6 |
| L9-AV8-R80 | 13.5 | 23518 | 46.9 | 1.3 | 2.84% | 2.04e6 |

### *4.2.1 Effect of local Kolmogorov-scale AMR thresholds*

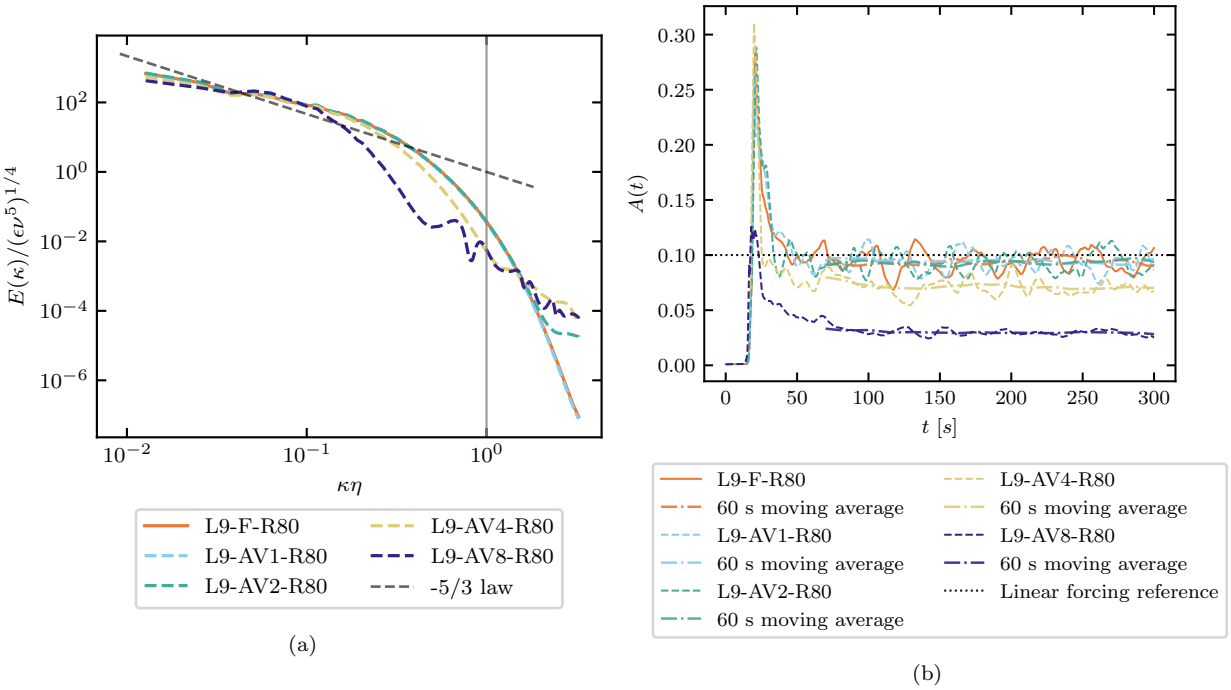
The following comparisons focus exclusively on the Kolmogorov-based adaptive refinement strategy. The four AMR cases use the same maximum refinement level ($\mathcal{L}9$), viscosity ($\nu = 0.001$ m$^2$s$^{-1}$), forcing and numerical method, differing only in the prescribed threshold $\Delta_r^{\max} = 1, 2, 4, 8$. This sequence is therefore interpreted as a controlled relaxation of the local grid-resolution requirement relative to the fixed-grid reference L9-F-R80.

Figure 7a presents the time-averaged 3D energy spectra $E(\kappa)$ normalized by Kolmogorov scales for the four AMR thresholds $\Delta_r^{\max} = 1$, 2, 4, and 8 alongside the fixed-grid reference L9-F-R80. The spectral distribution illustrates how statistical accuracy changes as grid adaptation is relaxed. For conservative thresholds ($\Delta_r^{\max} = 1$ and 2), the energy spectra remain close to the fixed-grid baseline across most of the resolved wavenumber range, including the inertial-range trend and the dissipative scales. Conversely, as the threshold is relaxed to $\Delta_r^{\max} = 4$ and 8, the loss of local spatial resolution introduces stronger filtering of fine-scale velocity gradients. This effect produces a premature cutoff in the dissipation range and is accompanied by reduced spectral energy over part of the resolved range.

Figure 7b tracks the temporal evolution of the forcing parameter $A(t)$, whose time-averaged values and relative errors are detailed in Table 8. The quantitative comparison shows that derivative-dependent observables are more sensitive to grid coarsening than integral quantities such as kinetic energy $\langle k \rangle$. While $\langle k \rangle$ exhibits a relative error of 12.07% for $\Delta_r^{\max} = 4$, the mean dissipation rate $\langle \epsilon \rangle$ reaches an error of 36.73%, which further increases to 76.49% for $\Delta_r^{\max} = 8$. Because $A \propto \epsilon / u_{\text{rms}}^2$ according to Eq. (7), this underestimation of viscous dissipation directly causes $A$ to drop from its target equilibrium value of 0.100 down to 0.072 and 0.030, respectively.

Table 8: Comparison between predictive consistency targets, simulation-averaged turbulence parameters, and integrated spectral observables for $t \geq 70$ s using maximum refinement level $\mathcal{L}_{\max} = 9$ and viscosity $\nu = 0.001$ m$^2$s$^{-1}$ across four adaptive mesh refinement threshold criteria: $\Delta_r^{\max} = 1,\ 2,\ 4,\ 8$.

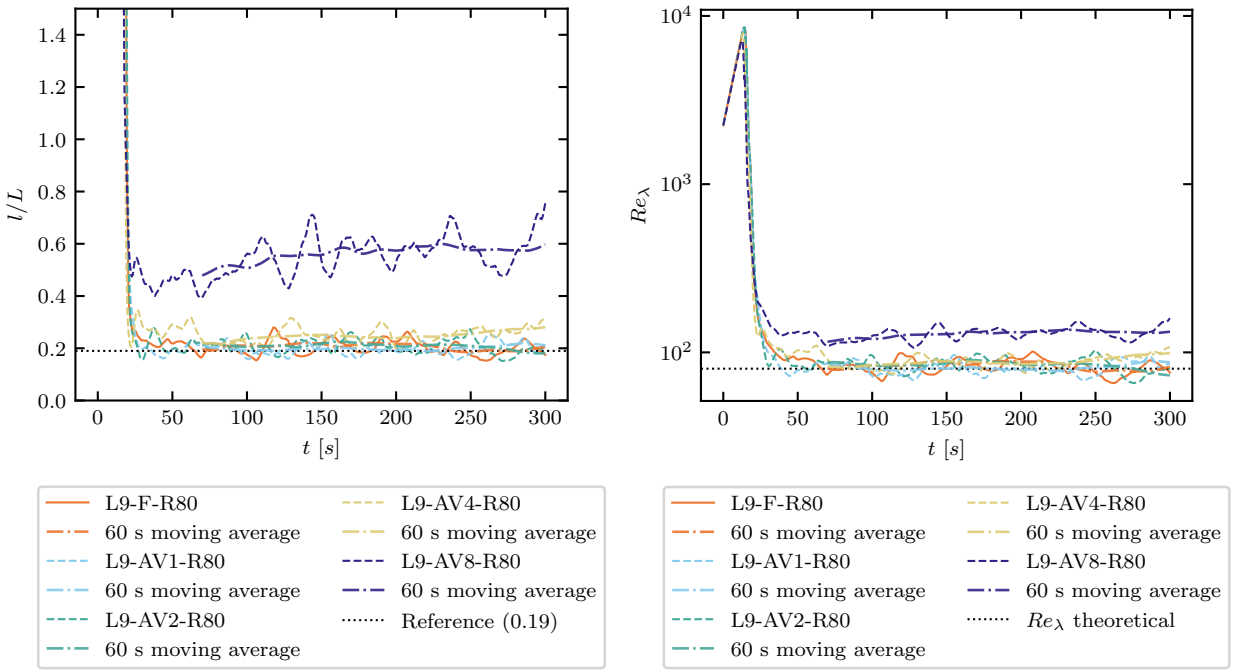
| Parameter | | $\Delta_r^{\max}$ 1 | 2 | 4 | 8 |
|---|---|---|---|---|---|
| $\langle k \rangle$ | Theo. | 0.19153 | 0.19153 | 0.19153 | 0.19153 |
| | Num. | 0.18659 | 0.19906 | 0.16841 | 0.15035 |
| | Error % | 2.58 | 3.93 | 12.07 | 21.50 |
| $\langle \epsilon \rangle$ | Theo. | 0.03831 | 0.03831 | 0.03831 | 0.03831 |
| | Num. | 0.03520 | 0.03702 | 0.02424 | 0.00901 |
| | Error % | 8.11 | 3.36 | 36.73 | 76.49 |
| $A$ | Theo. | 0.100 | 0.100 | 0.100 | 0.100 |
| | Num. | 0.094 | 0.093 | 0.072 | 0.030 |
| | Error % | 6.00 | 7.00 | 28.00 | 70.00 |
| $l/L$ | Theo. | 0.190 | 0.190 | 0.190 | 0.190 |
| | Num. | 0.199 | 0.209 | 0.249 | 0.564 |
| | Error % | 4.74 | 10.00 | 31.05 | 196.84 |
| $Re_\lambda$ | Theo. | 80.00 | 80.00 | 80.00 | 80.00 |
| | Num. | 81.19 | 84.46 | 88.45 | 129.46 |
| | Error % | 1.61 | 5.70 | 10.70 | 62.02 |
| $\eta$ | Theo. | 0.01271 | 0.01271 | 0.01271 | 0.01271 |
| | Num. | 0.01298 | 0.01282 | 0.01425 | 0.01825 |
| | Error % | 2.12 | 0.86 | 12.11 | 43.58 |
| $\Delta/\eta$ | Theo. | 0.96544 | 0.96544 | 0.96544 | 0.96544 |
| | Num. | 0.94544 | 0.95724 | 0.86118 | 0.67243 |
| | Error % | 2.07 | 0.85 | 10.80 | 30.35 |
| $\int E(\kappa)\, d\kappa$ | Theo. | 0.19153 | 0.19153 | 0.19153 | 0.19153 |
| | Num. | 0.18456 | 0.19650 | 0.16209 | 0.14145 |
| | Error % | 3.64 | 2.59 | 15.37 | 26.15 |
| $\int 2\nu\kappa^2 E(\kappa)\, d\kappa$ | Theo. | 0.03831 | 0.03831 | 0.03831 | 0.03831 |
| | Num. | 0.03559 | 0.03736 | 0.02373 | 0.00970 |
| | Error % | 7.09 | 2.46 | 38.04 | 74.68 |




(a) (b)

Fig. 7 Comparison of a) the energy spectra and b) temporal evolution of $A(t)$, for the fixed-grid reference L9-F-R80 and the Kolmogorov-based adaptive meshes with $\Delta_r^{\max} = 1$, 2, 4, and 8 at viscosity $\nu = 0.001$ m$^2$s$^{-1}$.

The complementary histories in Fig. 8 show analogous departures in the normalized length scale $l/L$ and the Taylor-microscale Reynolds number $Re_\lambda$ for the available post-processed adaptive cases. These signals confirm the trend reported in Table 8: the moderate threshold $\Delta_r^{\max} = 2$ remains closest to the fixed-grid reference, whereas the relaxed cases increasingly distort both the large-scale balance indicator $l/L$ and the Reynolds-number estimate derived from the resolved kinetic energy and dissipation.




(a) Normalized length scale $l/L$

(b) Taylor-microscale Reynolds number $Re_\lambda$

Fig. 8 Temporal evolution of complementary global indicators for the fixed-grid reference L9-F-R80 and the Kolmogorov-based adaptive meshes with $\Delta_r^{\max} = 1$, 2, 4, and 8 at viscosity $\nu = 0.001$ m$^2$s$^{-1}$

Figure 9 shows the time evolution of the active cell count for the different AMR threshold criteria, compared against fixed-grid references (dash-dotted lines). The simulation starts with a fully refined grid at the maximum level ($\mathcal{L}_{\max} = 9$). Depending on the threshold value, the mesh initially coarsens around the large-scale initial vortices before strongly re-refining to resolve the smaller vortical structures formed during the peak of kinetic energy and viscous dissipation. Once the flow reaches a statistically stationary state (at approximately $t \approx 70$ s), the active cell count stabilizes. This time history illustrates the dynamic geometric compression achieved by each threshold, whereas Table 7 summarizes the associated clock-time computational costs.

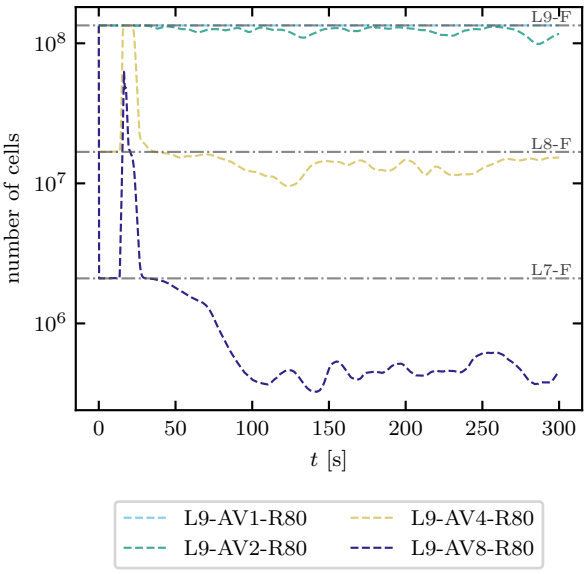



Fig. 9 Number of active cells as a function of time for the Kolmogorov-based adaptive meshes with $\Delta_r^{\max} = 1$, 2, 4, and 8 at viscosity $\nu = 0.001$ m$^2$s$^{-1}$. Dash-dotted lines indicate the equivalent fixed grids at levels 7, 8, and 9.

Thresholds $\Delta_r^{\max} = 4$ and 8 reduce the mean active cell count to 38.2 and 13.5 million and the execution time to 175.6 and 46.9 h, respectively, compared with 134.2 million cells and 318.3 h for the fixed grid (Table 7). These savings are accompanied by larger errors in dissipation and global-balance indicators. Conservative configurations with $\Delta_r^{\max} = 1$ and 2 provide the closest AMR representation of the resolved cascade, energy spectrum and global scaling parameters, keeping most global and spectral errors below approximately 10%. However, because globally homogeneous turbulence requires widespread fine resolution across the domain, maintaining high fidelity through AMR yields no computational speedup in the present configuration; instead, tree-management overhead increases total time relative to the uniform grid. The $\Delta_r^{\max} = 1$ case provides the closest AMR approximation to the fixed-grid reference, whereas $\Delta_r^{\max} = 2$ appears as the most practical high-fidelity threshold if a small statistical degradation is acceptable. The relaxed thresholds should therefore be restricted to qualitative or exploratory evaluations rather than high-fidelity turbulence characterization.

The four-threshold sequence should be read as a controlled relaxation experiment. If the sub-Kolmogorov adaptive case and the moderately relaxed cases reproduce $A(t)$, $l/L$, $Re_\lambda$, and the spectrum within the uncertainty of the fixed-grid reference, then some adaptive coarsening may be acceptable for this solver and Reynolds-number range. If a relaxed threshold reproduces the spectrum but not the global balance indicators, the missing information is not merely a high-wavenumber plotting artifact; it affects the statistically stationary dynamics of the resolved flow.

## 5 Discussion

The differences in $A(t)$, $l/L$, and $Re_\lambda$ between calculations with comparable energy spectra show that geometric resolution alone does not characterize the effect of mesh filtering. On adaptive meshes, the local cutoff also varies in time, linking the retained scales to the evolution of the refinement criterion.

A first key-point of the previous analysis is that the spectral agreement worsens as the grid resolution increases beyond $\Delta/\eta > 1$. Even if the energy spectrum seems to reach grid independence for resolutions smaller than this threshold, other turbulence features might vary when using finer grids. If the small-scales are under-resolved the error can feed back on the global statistics, altering the forcing-dissipation balance.

A second consequence is that the local coarsening threshold controls which structures are retained in the resolved field. In the present AMR sequence, increasing $\Delta_r^{\max}$ does not simply reduce the cell count; it changes the effective spatial filtering applied by the adaptive mesh. Moreover, using a relaxed refinement criterion can lead to excessive local coarsening, losing the scales representation at that time and affecting the transient evolution of the flow.

Adaptive implicit-LES studies show that filtering-induced dissipation can represent unresolved-scale effects within an appropriate operating range [5]. The present results emphasize that retaining this statistical fidelity under coarsening must be checked through both spectral and global indicators.

The present results also suggest practical fidelity checks for finite-volume turbulence simulations. The following conditions should be reached to increase the reliability of a simulation: (i) adequate dissipative-scale resolution, expressed for example through $\Delta/\eta$; (ii) correct global forcing-dissipation balance, measured through ratios such as $A(t)$; (iii) grid convergence of flow spatial scales metrics such as $l/L$ and $Re_\lambda$; and (iv) energy spectrum consistency with the integrated magnitudes.

Finally, although the present work focuses on homogeneous isotropic turbulence, the underlying numerical issue is likely to remain relevant in more complex turbulent configurations. In any finite-volume simulation, the grid spacing acts as an implicit filter, and the information lost below that scale may modify the resolved dynamics in ways that are not fully predictable from nominal resolution alone.

## 6 Conclusions

In the present finite-volume simulations of forced homogeneous isotropic turbulence, grid refinement changes the dissipation and global statistics more strongly than it changes the energy spectrum. The fixed-grid and AMR comparisons quantify this sensitivity for the Basilisk solver and forcing framework studied here.

The forcing-balance parameter $A(t)$, the ratio $l/L$, and the Taylor-scale Reynolds number $Re_\lambda$ respond to errors in the resolved velocity gradients through their dependence on dissipation. For the present solver and within the Reynolds-number range studied, a slightly sub-Kolmogorov spacing ($\Delta/\eta \approx 0.95$) was required on fixed grids to recover grid independence of the global forcing–dissipation balance indicators.

The comparison between fixed-grid and adaptive-grid simulations further shows that adaptive coarsening acts as a dynamic filtering strategy. Relaxing the allowed local ratio $\Delta/\eta_{\text{local}}$ modifies which structures are retained in the resolved field and therefore alters the effective representation of the turbulent cascade. The AMR results indicate that a conservative threshold of $\Delta_r^{\max} = 1$ forces the grid refinement to full capacity, achieving the maximum possible resolution. The setup with $0.5 < \Delta_r < 2$ preserves the energy distribution

and a comparable accuracy, even when the grid is sometimes coarsened locally. The aforementioned thresholds provide the closest statistical agreement with the fixed-grid reference. The relaxed thresholds $\Delta_r^{\max} = 4$ and 8 apply a more aggressive coarsening, reducing the computational cost significantly but introducing numerical errors that affect the turbulence dynamics too much to achieve a high-fidelity characterization of the flow.

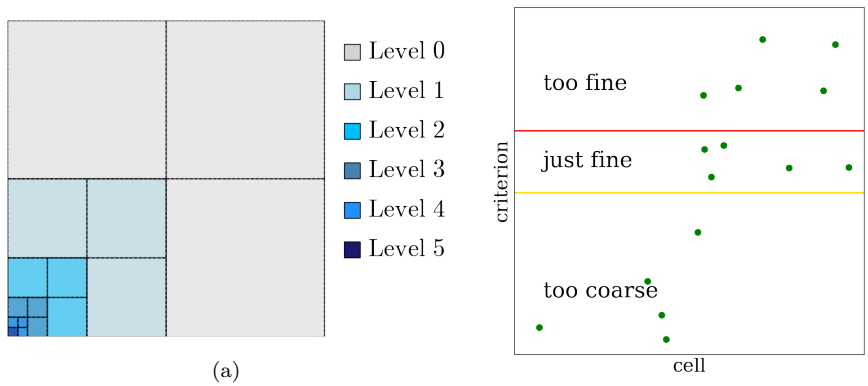
Overall, this work assesses how spectral and non-spectral diagnostics complement each other in evaluating the fidelity of turbulence simulations. When a grid resolution of $\Delta/\eta = 1$ is employed, the error measures remain bounded below 10%, generally reaching a very good agreement with the reference theoretical values. Refinement beyond this threshold introduces some small-scale structures that affect the total energy and dissipation but does not have significant impact on the accuracy of $A$, $l/L$, or $Re_\lambda$. Future work should include exploring a broader range of flow regimes, including more non-ideal turbulent conditions, to assess the impact of anisotropic dynamics.

## A Details of the mesh and the Adaptive Mesh Refinement Algorithms

### A.1 Tree-Based Grid Hierarchy

The hierarchical tree-based mesh structure in Basilisk originates from a single parent cell level-0 ($\mathcal{L}0$) spanning the entire computational domain of size $L$. Each subsequent refinement level divides the existing cells by a factor of two in each spatial direction. Therefore, a cell at a generic refinement level $\mathcal{L}$ possesses a grid spacing of $\Delta = L/2^{\mathcal{L}}$. A two-dimensional schematic representation of this grid hierarchy is illustrated in Figure 10a.

This structure enables computationally efficient adaptive mesh refinement (AMR), which is used here to adjust the local resolution according to a prescribed criterion. The procedure is governed by two main parameters: the maximum refinement level and the refinement criterion. The latter is defined through an error indicator evaluated in each cell of the computational domain. Cells for which the estimated error falls below a lower threshold are regarded as over-resolved and are therefore coarsened, whereas cells for which the error exceeds an upper threshold are considered under-resolved and are refined. Figure 10b schematically illustrates representative values of the error indicator together with the prescribed refinement bounds, which guide the dynamic refinement and coarsening of the grid throughout the simulation.




(a) (b)

Fig. 10 Overview of the grid framework features: (a) Two-dimensional sketch of the tree-based mesh hierarchy, showing cell size halving per refinement level from the root cell (level 0); (b) Dynamic mesh refinement and coarsening algorithm, where criterion evaluation determines cell refinement, retention, or coarsening (adapted from [32])

### A.2 Local Kolmogorov-scale refinement

The adaptive simulations use a criterion based on a local estimation of the Kolmogorov scale, similarly to Eq. (14), as:

$$\eta_{\text{local}} = \left(\frac{\nu^3}{\epsilon_{\text{local}}}\right)^{1/4} \tag{20}$$

where $\nu$ is the kinematic viscosity of the fluid and $\epsilon_{\text{local}}$ is the viscous dissipation rate computed locally in each cell.

The local energy dissipation rate, is computed in each cell from the resolved velocity gradients as:

$$\epsilon_{\text{local}} = \nu \left(\frac{\partial u_i}{\partial x_j}\frac{\partial u_i}{\partial x_j}\right) \tag{21}$$

where $\nu$ represents the kinematic viscosity of the fluid, and $u_i$ denotes the velocity components in the three spatial directions $x_j$. At the discrete level, the spatial derivatives are approximated using second-order centered finite differences.

Finally, the mesh refinement indicator, proposed in [20], is defined as the non-dimensional ratio between the local cell size and the local estimation of the smallest turbulent scales:

$$\Delta_r = \frac{\Delta}{\eta_{\text{local}}} \tag{22}$$

This indicator is evaluated dynamically by the mesh adaptation algorithm to keep the resolution ratio within the prescribed range between $\Delta_r^{min}$ and $\Delta_r^{max}$. The mesh is locally refined if the ratio exceeds the upper limit ($\Delta_r > \Delta_r^{max}$) and coarsened if it falls below the lower threshold ($\Delta_r < \Delta_r^{min}$). This criterion is motivated by the Kolmogorov-scale DNS guidelines discussed in [23], but its adequacy must still be verified through the spectral and statistical diagnostics used in the main text.

## B Details of the Fourier Analysis and 3D FFT Spectral Calculations

The spectral description of homogeneous turbulence allows for the decomposition of flow quantities in terms of wavenumbers and frequencies, or equivalently length and time scales. Specifically, the velocity field can be represented in terms of the wavenumber vector $\vec{\kappa} = (\kappa_1, \kappa_2, \kappa_3)$, linking physical scales to spatial frequencies. For a real-valued velocity field $u_i(\vec{x})$ defined over a uniform domain of $N_1 \times N_2 \times N_3$ nodes, the discrete Fourier transform $\hat{u}_i(\vec{\kappa})$ is given by:

$$\hat{u}_i(\vec{\kappa}) = \frac{1}{N_1 N_2 N_3} \sum_{m=0}^{N_1-1} \sum_{l=0}^{N_2-1} \sum_{p=0}^{N_3-1} u_i(\vec{x}) e^{-i(\kappa_1 x_m + \kappa_2 y_l + \kappa_3 z_p)} \tag{23}$$

where $\vec{x} = (x_m, y_l, z_p)$ represents the spatial coordinates. Due to the real-valued nature of the velocity components, the Fourier coefficients satisfy the conjugate symmetry condition $\hat{u}_i(\vec{\kappa}) = \hat{u}_i^*(-\vec{\kappa})$, where the asterisk denotes the complex conjugate.

The spatial structure of the turbulent fluctuations is formally described by the two-point velocity correlation tensor in physical space:

$$R_{ij}(\vec{r}) = \langle u_i'(\vec{x}) u_j'(\vec{x} + \vec{r}) \rangle \tag{24}$$

where $\vec{r}$ is the separation vector and $u_i'$ represents the velocity fluctuations, and the brackets $\langle \dots \rangle$ denote the volume average over the entire computational domain under the assumption of spatial homogeneity. In spectral space, the velocity correlation tensor [29] $\Phi_{ij}(\vec{\kappa})$ is obtained via the Fourier transform of $R_{ij}(\vec{r})$, which relates to the velocity coefficients as:

$$\Phi_{ij}(\vec{\kappa}) = \hat{R}(\vec{\kappa}) = \langle \hat{u}_i'(\vec{\kappa}) \hat{u}_j'^*(\vec{\kappa}) \rangle \tag{25}$$

The three-dimensional energy spectrum is obtained from the correlation tensor $\Phi_{ij}(\vec{\kappa})$. For isotropic turbulence, the correlation tensor trace $\Phi_{ii}(\vec{\kappa})$ depends solely on the wavenumber magnitude $\kappa = |\vec{\kappa}|$. In numerical implementations using standard Fast Fourier Transform libraries (such as FFTW), the outputs are typically unnormalized [21]. To account for this, the discrete trace of the correlation tensor is computed as:

$$\Phi_{ii}(\vec{\kappa}) = \frac{\hat{u}_i'(\vec{\kappa})}{N^3} \frac{\hat{u}_i'^*(\vec{\kappa})}{N^3} = \frac{|\hat{u}_i'(\vec{\kappa})|^2}{N^6} \tag{26}$$

assuming a grid where $N_1 = N_2 = N_3 = N$.

Finally, to compute the one-dimensional energy spectrum $E(\kappa)$, a numerical spherical integration of $\Phi_{ii}(\vec{\kappa})$ is performed. The continuous shell integration is discretized by partitioning the wavenumber domain into concentric spherical shells (or bins) of a constant width $\Delta\kappa$. The spectral energy contribution within a shell centered at $\kappa_{bin}$ is obtained by summing the discrete modes whose magnitudes fall within the shell bounds:

$$E(\kappa_{bin}) = \frac{1}{\Delta\kappa} \sum_{\kappa_{bin} - \frac{\Delta\kappa}{2} \le |\vec{\kappa}| \le \kappa_{bin} + \frac{\Delta\kappa}{2}} \frac{1}{2} \Phi_{ii}(\vec{\kappa}) \tag{27}$$

This discrete summation yields the spectral energy distribution presented in this work.

## C Choice of the moving average time window

To isolate the underlying trends of the turbulent statistics from the low-frequency oscillations inherent to the dynamic equilibrium state, a moving average filter was applied to both the volume-averaged turbulent kinetic energy $\langle k \rangle$ and the dissipation rate $\langle \epsilon \rangle$. The 60 s smoothing window was selected to approximately match the dominant period of 57.5 s identified in the late-time signals.

This choice is supported by a spectral analysis of the time series within the statistically stationary regime ($t \geq 70$ s). As illustrated in Fig. 11, the discrete power spectra $|F(k)|$ and $|F(\epsilon)|$ obtained via a Fast Fourier Transform (FFT) reveal that the dominant oscillation frequency for both variables is $f_0 = 0.0174$ Hz, which corresponds to a characteristic integral-temporal scale of $\tau_0 = 1/f_0 \approx 57.5$ s.

In contrast, the computed integral time scale of the turbulence estimated via Eq. (8) yields $\tau \approx 3.43$ s, consistent with the theoretical value of 3.33 s for this isotropic configuration.

Consequently, selecting $T_{\text{avg}} = 60$ s ensures that the filtering window simultaneously satisfies two criteria: first, $T_{\text{avg}} \approx \tau_0$, thereby effectively modulating and filtering out the large-scale temporal oscillations originating from the global domain; and second, $T_{\text{avg}} \gg \tau$, which guarantees that a sufficient number of turnover cycles ($\sim 17.5$ integral time scales) are included within each local average window, yielding a statistically converged mean.

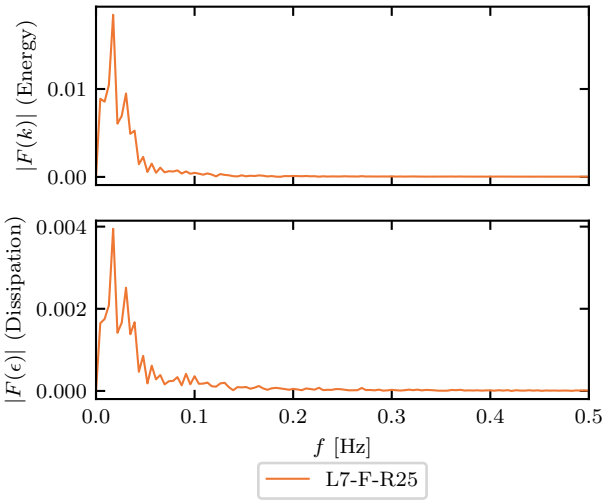



Fig. 11 Power amplitudes of the Fast Fourier Transform (FFT) for the volume-averaged turbulent kinetic energy $|F(k)|$ and dissipation rate $|F(\epsilon)|$ within the statistically stationary regime ($t \geq 70$ s). The primary energetic peak at $f_0 = 0.0174$ Hz ($\tau_0 \approx 57.5$ s) governs the large-scale periodic modulations of the domain, justifying the selection of the 60 s moving average window

## Statements and Declarations

### Funding and Acknowledgments

This work was supported by the National Scientific and Technical Research Council (CONICET) and the Universidad Nacional de Rosario (UNR) through projects 80020250200018UR and 80020220600038UR. The Pirayu cluster used for the computations was acquired with funds from the Santa Fe Agency for Science, Technology and Innovation (ASACTEI), Government of the Province of Santa Fe, through Project AC-00010-18, Resolution No. 117/14, and forms part of the National System of High-Performance Computing of the Argentine Ministry of Science and Technology.

### Use of AI-assisted tools

An AI language model was used for adapting the manuscript to LaTeX format. The authors are responsible for the accuracy and integrity of the final manuscript.

### Competing Interests

The authors have no conflicts to disclose.

### Author Contributions

María Clara Cortizo Carbone: Investigation, Formal analysis, Data curation, Visualization, Writing – review & editing. Juan Cruz Catalano: Writing – review & editing. César M. Venier: Writing – review & editing. Santiago Márquez Damián: Writing – review & editing. César I. Pairetti: Conceptualization, Methodology, Writing – original draft, Writing – review & editing. All authors contributed to the discussion of the results and to the review and editing of the text.

### Data Availability

The data that support the findings of this study are available from the corresponding author upon reasonable request.

## References

1. Basilisk: Forced isotropic turbulence in a triply-periodic box (2026). URL `https://basilisk.fr/src/examples/isotropic.c`
2. Bell, J.B., Colella, P., Glaz, H.M.: A second-order projection method for the incompressible navier–stokes equations. Journal of Computational Physics **85**(2), 257–283 (1989)
3. Cadieux, F., Sun, G., Domaradzki, J.A.: Effects of numerical dissipation on the interpretation of simulation results in computational fluid dynamics. Computers & Fluids **154**, 256–272 (2017)
4. Courant, R., Friedrichs, K., Lewy, H.: Über die partiellen differenzengleichungen der mathematischen physik. Mathematische annalen **100**(1), 32–74 (1928)

5. De Stefano, G.: Wavelet-based adaptive implicit les/under-resolved dns of forced isotropic turbulence. Theoretical and Computational Fluid Dynamics **39**(5), 42 (2025). https://doi.org/10.1007/s00162-025-00762-0
6. Frigo, M., Johnson, S.G.: The design and implementation of FFTW3. Proceedings of the IEEE **93**(2), 216–231 (2005). Special issue on "Program Generation, Optimization, and Platform Adaptation"
7. Frisch, U.: Turbulence: the legacy of AN Kolmogorov. Cambridge University Press (1995)
8. Geier, M., Lenz, S., Schönherr, M., Krafczyk, M.: Under-resolved and large eddy simulations of a decaying taylor–green vortex with the cumulant lattice boltzmann method. Theoretical and Computational Fluid Dynamics **35**(2), 169–208 (2021). https://doi.org/10.1007/s00162-020-00555-7
9. Gimenez, J.M., Sívori, F.M., Larreteguy, A.E., Montaño, S.I., Aguerre, H.J., Nigro, N.M., Idelsohn, S.R.: A multiscale pseudo-dns approach for solving turbulent boundary-layer problems. Computer Methods in Applied Mechanics and Engineering **437**, 117,804 (2025). https://doi.org/10.1016/j.cma.2025.117804
10. Jeong, J., Hussain, F.: On the identification of a vortex. Journal of fluid mechanics **285**, 69–94 (1995). https://doi.org/10.1017/S0022112095000462
11. Kim, J., Leonard, A.: The early days and rise of turbulence simulation. Annual Review of Fluid Mechanics **56**, 21–44 (2024). https://doi.org/10.1146/annurev-fluid-120821-025116
12. Kolmogorov, A.N.: Dissipation of energy in the locally isotropic turbulence. In: Dokl. Akad. Nauk. SSSR, vol. 32, pp. 19–21 (1941)
13. Kolmogorov, A.N.: The local structure of turbulence in incompressible viscous fluid for very large reynolds. Numbers. In Dokl. Akad. Nauk SSSR **30**, 301 (1941)
14. Kolmogorov, A.N.: A refinement of previous hypotheses concerning the local structure of turbulence in a viscous incompressible fluid at high reynolds number. Journal of Fluid Mechanics **13**(1), 82–85 (1962)
15. Lagrée, P.Y., Staron, L., Popinet, S.: The granular column collapse as a continuum: validity of a two-dimensional Navier–Stokes model with a $\mu$ (I)-rheology. Journal of Fluid Mechanics **686**, 378–408 (2011). https://doi.org/10.1017/jfm.2011.335
16. Li, D., Yang, L., Zhang, K., Luo, K., Fan, J.: Mixed subfilter-scale models for large-eddy simulation of decaying isotropic turbulence using an artificial neural network. Computers & Fluids **289**, 106,557 (2025). https://doi.org/10.1016/j.compfluid.2025.106557
17. Lundgren, T.S.: Linearly forced isotropic turbulence. Annual Research Briefs - Center for Turbulence Research (2003)
18. Moin, P., Chan, W.H.R.: Fundamentals of Turbulent Flows. Cambridge University Press (2024)
19. Moin, P., Mahesh, K.: Direct numerical simulation: a tool in turbulence research. Annual review of fluid mechanics **30**(1), 539–578 (1998)
20. Pairetti, C.I.: Modelización de flujos turbulentos multifásicos aplicada al diseño de sistemas inyectores de nafta en motores de combustión interna. Ph.D. thesis, Universidad Nacional de Rosario (2019)
21. Papadimitriou, C.H.: Optimality of the fast fourier transform. Journal of the ACM (JACM) **26**(1), 95–102 (1979)
22. Podvigina, O., Pouquet, A.: On the non-linear stability of the 1: 1: 1 ABC flow. Physica D: Nonlinear Phenomena **75**, 471–508 (1994). https://doi.org/10.1016/0167-2789(94)00031-X
23. Pope, S.B.: Turbulent flows. Cambridge University Press (2000)
24. Popinet, S.: Gerris: a tree-based adaptive solver for the incompressible Euler equations in complex geometries. Journal of Computational Physics **190**(2) (2003). https://doi.org/10.1016/S0021-9991(03)00298-5
25. Popinet, S.: An accurate adaptive solver for surface-tension-driven interfacial flows. Journal of Computational Physics **228**(16) (2009). https://doi.org/10.1016/j.jcp.2009.04.042
26. Popinet, S.: The basilisk code (2014). URL `https://basilisk.fr`. Accessed 6 October 2026
27. Rivière, A.: Bubble deformation and fragmentation in turbulence. Ph.D. thesis, Université Paris sciences et lettres (2024)
28. Rosales, C., Meneveau, C.: Linear forcing in numerical simulations of isotropic turbulence: Physical space implementations and convergence properties. Physics of Fluids **17**(9) (2005). https://doi.org/10.1063/1.2047568
29. Sagaut, P., Deck, S., Terracol, M.: Multiscale and Multiresolution Approaches in Turbulence. Imperial College Press (2006)
30. Tan, J., Jin, G.: An artificial neural network model for recovering small-scale velocity in large-eddy simulation of isotropic turbulent flows. Physics of Fluids **36**(8), 085,170 (2024). https://doi.org/10.1063/5.0221039
31. Trias, F.X., Ruano, J., Duben, A., Gorobets, A.: A rational length scale for large-eddy simulation of turbulence on anisotropic grids. Physics of Fluids **37**(8), 085,239 (2025). https://doi.org/10.1063/5.0277423
32. Van Hooft, J.A., Popinet, S., Van Heerwaarden, C.C., Van der Linden, S.J., De Roode, S.R., Van de Wiel, B.J.: Towards adaptive grids for atmospheric boundary-layer simulations. Boundary-layer meteorology **167**(3), 421–443 (2018)
33. Yeung, P., Sreenivasan, K., Pope, S.: Effects of finite spatial and temporal resolution in direct numerical simulations of incompressible isotropic turbulence. Physical Review Fluids **3**(6), 064,603 (2018)